

Allpix-Squared Simulations of Multi-element Germanium Detectors for Synchrotron Applications

T. Saleem,^{a,1} F.J. Iguaz,^a F. Orsini^a

^aSOLEIL Synchrotron,
L'Orme des Merisiers, Saint-Aubin BP 48, Gif-sur-Yvette, 91190 France

E-mail: tasneem.saleem@synchrotron-soleil.fr

ABSTRACT: X-rays spectroscopy experiments at synchrotron facilities were limited for many years by the maximum input-count rate and the signal-to-background ratio of germanium fluorescence detectors. These limitations are in part related to the germanium semiconductor device, and more generally depending on the detector (sensor) configuration and its response to the incident photon flux at different energies. In order to understand and quantify such limitations, physics simulation of the detector response is a powerful tool to provide guidelines for designing, prototyping and improving detectors, as well as modelling experimental environments, which reduces time and cost of development. For this purpose, a full-simulation chain, based on validated well-known simulation codes, has been implemented and adapted to germanium parameters. This simulation chain and specific detector performance studies, including quantification of charge sharing, as well as signal-to-background ratio at different energies, are presented in this paper. Moreover, the simulation chain is calibrated and validated using experimental results obtained at one of the beamlines at SOLEIL Synchrotron.

KEYWORDS:

X-ray detectors

Instrumentation for synchrotron radiation accelerators

Detector modelling and simulations I (interaction of radiation with matter, interaction of photons with matter, interaction of hadrons with matter, etc)

Detector modelling and simulations II (electric fields, charge transport, multiplication and induction, pulse formation, electron emission, etc)

¹Corresponding author.

Contents

1	Introduction	1
2	Multi-element germanium detector specifications	2
3	Physics processes and simulation flow	3
3.1	Energy Deposition: Geant4 simulation	5
3.2	Electrostatic field modeling: COMSOL Multiphysics® simulation	5
3.3	Charge carrier drift and signal induction	8
3.4	Signal digitization and energy spectrum	9
4	Simulation of multi-element germanium detector performance	9
4.1	Quantification of the charge sharing effect with and without collimator	10
4.2	Study of the detector performance at different beam energies	12
5	Experimental measurements to calibrate simulation results	14
5.1	On-beamline measurements	14
5.2	Comparison between simulation and experimental results	16
6	Conclusion and Outlook	18

1 Introduction

X-rays spectroscopy techniques are commonly used on several beamlines at synchrotron facilities to perform experiments in a large field of sciences such as Physics, Chemistry, Environmental Sciences, Biology, and Surface Material Science. During many years, the experiments were generally limited by the sensitivity of the fluorescence detectors where the maximum input-count rate and energy resolution capabilities of the detector are of primary importance. With the current and coming upgrade of synchrotron light sources with higher brilliance, it becomes a major challenge to overcome the limitations of current commercial detectors available on the market. For that purpose, the understanding of detector performances and limitations including its associated front-end electronics remains essential.

The objective of this work is to build a full-simulation chain adapted to multi-element germanium detectors [1–3] to study their response to incident photons, in the energy range from 5 keV to 100 keV, taking into account a beamline sample environment at synchrotron facilities. For realistic modeling of the multi-element germanium detector response, a simulation chain combining 3D electrostatic field simulation using COMSOL Multiphysics® tools and allpix-squared simulations [4] is used. It's worth mentioning that the allpix-squared is a generic simulation framework originally developed to study the performance of silicon detectors. This work is the first application of allpix-squared for the simulation of germanium detectors.

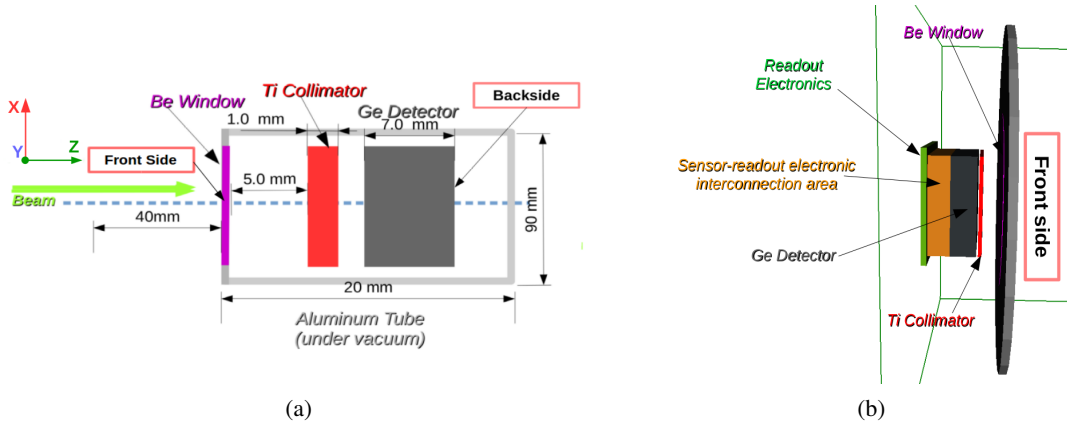


Figure 1: (a) Schematic representation of the multi-element germanium detector under study showing the different simulated components, where the frontside is the one facing the incident X-rays (b) Visualization of the multi-element germanium detector geometry after implementation in allpix-squared framework.

After the presentation of the simulation flow and specific adaptation to germanium material, the simulation chain is applied to a current germanium detector in use at the SAMBA beamline [5] of the SOLEIL synchrotron. The detector performance as well as its limitations at different beam energies are simulated. In a second step, the simulation is ‘calibrated’ by comparing the predicted performance obtained by simulation with real measurements recorded during a beam test on a beamline. Finally, comparison between simulations and real data is discussed with possible improvements for future developments.

2 Multi-element germanium detector specifications

The multi-element germanium detector used as model for this simulation is a commercial germanium detector (Model: Canberra EGPS 30×30×7-36 PIX). Figure 1 (a) presents a general schematic of the multi-element germanium detector under study and shows the different simulated components. The detector consists of a high-purity germanium crystal with an active area of 30 mm × 30 mm and a thickness of 7 mm. The germanium crystal is located at 5 mm behind a 125 μm thick Beryllium window with a diameter of 46 mm. On the backside, the crystal is segmented into 6 × 6 pixel contacts, with a pixel size of 4.2 mm × 4.2 mm. The detector under study has a titanium (Ti) collimator of 1 mm thick that is placed at 1 mm in front of the germanium crystal. The collimator has 36 square holes each of 4.2 mm long and a pitch of 5 mm. The detector is surrounded by an Aluminium tube of 90 mm (inner) diameter and 2 mm thick. The Aluminium tube keeps the detector under vacuum. The detector operates in electron collection mode at a nominal bias voltage of -800 V.

Using the detector geometry described above, the multi-element germanium detector geometry has been simulated using allpix-squared framework and is shown in Figure 1 (b). In this figure, the Beryllium window is in purple, and the frontside of the Aluminium tube is in grey. The surrounding tube is invisible in this figure for better visualization of the inner parts of the detector. Inside

the Aluminium tube, the collimator is in red, the germanium sensor in black, the sensor-readout electronic interconnection area in orange and the readout electronic in green.

3 Physics processes and simulation flow

In this section, a brief explanation of the physics processes resulting from X-ray interaction inside a typical germanium detector, followed by a full description of the simulation flow used in this work are presented.

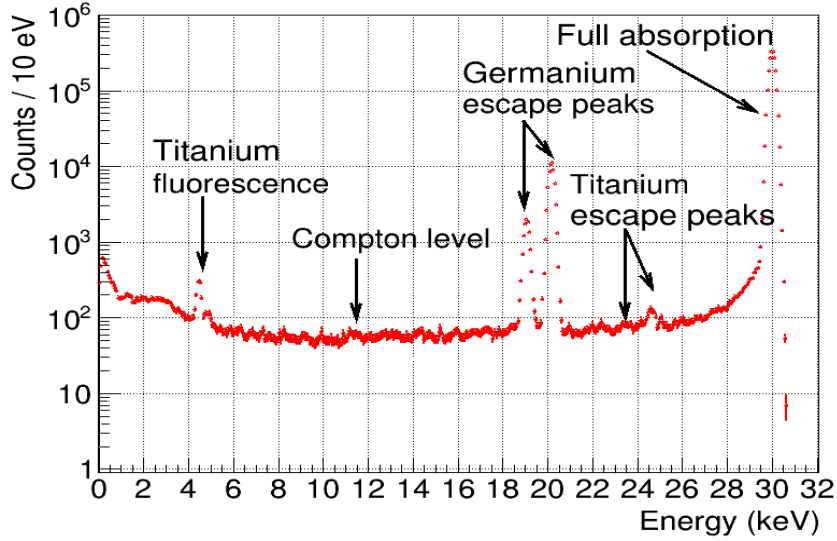


Figure 2: Example of a simulated energy distribution deposited by 30 keV photons and measured by a germanium detector equipped with a titanium collimator. All peaks and regions of interest that correspond to different physics processes are identified.

In the energy range (5-100 keV), the photoelectric interaction is the dominant process. In this case, the photo-electron loses most of its energy by ionization but the remission of germanium fluorescence X-rays (at energies of 9.88 and 10.98 keV, corresponding to K_α and K_β emission lines of germanium) is also possible for energies above 11 keV, as shown with the example of Figure 2. These germanium fluorescence X-rays may be reabsorbed in the germanium crystal, creating another energy deposit, or escape. Events with two separated energy deposits will probably spread over multiple pixels, resulting in charge sharing events called *fluorescence events* (following the name convention of [6]). All energy deposits promote electrons to the conduction band, creating clouds of electron and holes. By applying a bias voltage across the crystal, charge carriers drift from the frontside to the segmented backside, where they induce signals in the readout. In our case, holes drift to the frontside and electrons to the backside. While drifting, charge clouds widen due to diffusion effects and carriers drifting to the backside may spread and induce signals over multiple pixels, resulting in charge sharing events called *split events*. Charge shared events (either *fluorescence* or *split events*) reduce the intensity of the full absorption peak and increase the Compton level referred to Figure 2), and then initial X-ray energy is not fully reconstructed. Induced signals

Table 1: List of simulation steps, corresponding module in allpix-squared framework and their main parameters.

Step	allpix-squared module	Parameter	Symbol	Value
Geant4	<i>DepositionGeant4</i>	Electron-hole pair energy	W	2.9 eV
		Fano factor	F	0.112
		Max. step length		1 μm
Drift	<i>GenericPropagation</i>	Temperature	T	77 K
		Electron mobility	μ_e^0	38536 $\text{cm}^2/\text{V/s}$
		- field correction	E_e^0	53.8 V/mm
		- temperature correction	β_e	0.641
		Hole mobility	μ_h^0	61215 $\text{cm}^2/\text{V/s}$
		- field correction	E_h^0	18.2 V/mm
		- temperature correction	β_h	0.662
		Charge per step		100 e/h
		Time per step		1 ns
		Integration time		200 ns
Transfer	<i>InducedTransfer</i>	Weighting potential induction matrix		3×3
Digitization	<i>DefaultDigitizer</i>	Electron noise	ENC	31 e
		Threshold		100 e
Spectrum	[Offline analysis]	Dead time		1430 ns
		Time resolution		300 ns

are then digitized and finally collected into a full energy spectrum by a Digital Pulse Processor (DPP). In our case, the titanium collimator situated at the frontside of the germanium crystal makes also possible the absorption of titanium fluorescence (at energies of 4.51 and 4.93 keV, K_α and K_β lines) in the germanium crystal and, with less probability, of Compton scattered photons from titanium collimator. The result shown on Figure 2 is obtained by simulating 2×10^6 photons. About 94.5% of these photons have the full 30 keV deposited in one pixel (full absorption). While in the remaining cases, energy is either shared with other pixels or lost either by fluorescence or by Compton scattering.

To take into account the previously mentioned physics processes, the simulation flow is divided into five parts: simulation of the X-ray interaction with matter, simulation of the charge carrier cloud drift using a three-dimensional drift field map, signal induction in the segmented backside, signal digitization and energy spectrum creation in the DPP. All these steps are done through different modules developed in the allpix-squared framework [4], but using a modified version that has been adapted to implement germanium properties. The electric field map simulation has externally been provided by COMSOL Multiphysics®, and the specific features of DPP have been implemented in the post-simulation analysis. A list of simulation steps in allpix-squared modules and main simulation parameters is provided in Table 1.

3.1 Energy Deposition: Geant4 simulation

The interaction of photons with the germanium crystal is simulated by the *Geant4* library [7] using the *DepositionGeant4* module. This allpix-squared module has been adapted to germanium detectors by modifying the base material from silicon to germanium. Polarization effects have been included by explicitly using *G4EmLivermorePolarizedPhysics* class of Geant4 (version 4.10.6), which also uses low energy models based on Livermore data libraries for interactions of photons with matter. These interaction models are accurate for photon energies between 250 eV up to 100 GeV and can be applied down to 100 eV with a reduced accuracy [8]. The energy deposits in the germanium sensors are translated into charge carriers with a conversion factor of 2.9 eV per electron-hole pair and a primary charge fluctuation modeled by a Fano factor of 0.112 [9].

In this work, a photon beam has been simulated for two different cases:

- A uniform square shape beam along the positive z-axis, perpendicular to the detector, used to directly illuminate the multi-element germanium detector for charge sharing studies, presented in Section 4. The beam cross section is modeled by two independent uniform distributions along each perpendicular axis.
- A Gaussian shape beam along the x-axis, linearly polarized along z-axis, to irradiate a reference sample to study the resulting fluorescence detected by the detector, located perpendicular to the beam. This case, presented in Section 5, is used to replicate the experimental beam conditions and to validate the simulation results. The beam cross section is modeled by two independent Gaussian distributions along each perpendicular axis.

3.2 Electrostatic field modeling: COMSOL Multiphysics® simulation

The non-linear variation of the electric field in three dimensions, within the device structure, can affect the behavior and the predicted performance of the detector. Due to that, a precise 3D electric field description is a crucial ingredient for a proper simulation and understanding of detector characteristics. Moreover, combining electrostatic field simulations with Monte Carlo methods enables realistic modeling of the detector response as shown in section 4.

The COMSOL Multiphysics® software provides a numerical technique to simulate the electric field using the Finite Element Method (FEM) if the practical dimensions and material properties of the device are given. COMSOL Multiphysics® is used in this work to formulate and solve the differential form of Maxwell's equations together with a set of initial and boundary conditions, and post-process the results to evaluate non-linear electric field components within the simulated device.

The workflow is as follows: first, the geometry is defined and parametrized; materials are assigned to the different volumes of the model; a semiconductor interface is chosen with the model's respective boundary and initial conditions; the element mesh is created; a solver is selected and subsequently, the results are computed. The phenomenon of avalanche breakdown in germanium sensor has been simulated under the basis of the known Okuto-Crowell Impact Ionization model [10]. This model requires eight parameters that are specific for each semiconductor material. While for silicon detectors these values are well known, for germanium detectors these values are rarely cited in the literature; the ones used for this work can be found here [10].

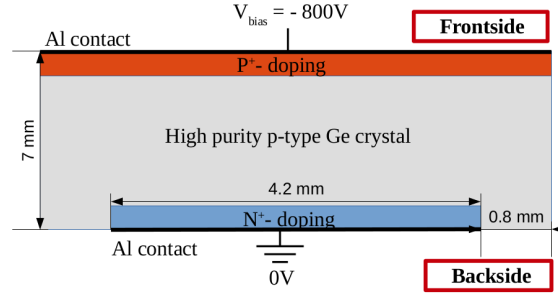


Figure 3: Schematic representation of the germanium sensor under study. The high purity germanium crystal is in gray. The N^+ -doped collection electrode (pixel region) of thickness $5 \mu\text{m}$ is in blue. The P^+ -doped region with a higher doping concentration of thickness of $10 \mu\text{m}$ is in red. A bias voltage of -800 V is applied at the frontside, and the pixel electrode is grounded.

For these simulations, the same detector geometry introduced previously in section 2 has been used. A more detailed schematic representation of the germanium sensor only is shown in Figure 3. The frontside (facing the incident X-rays) is Boron implanted (p^+ -doped electrode) while the backside (segmented side) is Phosphorus implanted (n^+ -doped). The inter-pixel spacing is equal to 800 microns wide. Aluminum contact of 300 nm has been evaporated on the implants (pixel surface) and on the frontside of the device. The corresponding voltages applied to the different collection electrodes are also shown in Figure 3. The detector works in electron collection mode.

The information about the different implanted regions is not available by the manufacturer since this type of information is usually confidential. Therefore, the doping profiles have been taken from [3], where typical values for n-type high purity germanium crystal and standard dopant concentration for pixels have been used. The simulation includes a single pixel cell with periodic boundary conditions which allow the field to be replicated over the entire sensor. For computing time and computer memory capability reasons, only 1 mm thick has been simulated. It has been verified that this thickness is sufficiently representative of the non-linear part of the electric field close to the pixel implants, and a linear part of the electric field is extrapolated for the remaining depth.

A visualization of the magnitude of the electric field in the three-dimensional model is shown in Figure 4 (a). A low electric field is present in the inter-pixel region as well as the central pixel region, as indicated by the blue region on the surface of the simulated pixel cell. In contrast, a high-field region is evolving around the pixel edge region. A cut through the collection electrode, perpendicular to the sensor surface is shown in Figure 4 (b). The electric field strength is higher close to the pn-junction around the collection electrode and decreases rapidly towards the sensor frontside.

Charge carrier concentration, as a function of the sensor depth, is shown in Figure 5, for in-pixel region (a) and inter-pixel region (b). Inside the pixel, the charge carrier distribution shows that electron concentration is higher at the backside implant (i.e., electrons are collected by the backside electrode). On the other hand, the hole concentration is lower at the side of the pixel, which is reflecting the fact that the sensor is reversed bias and working in an electron-collecting mode as foreseen by design.

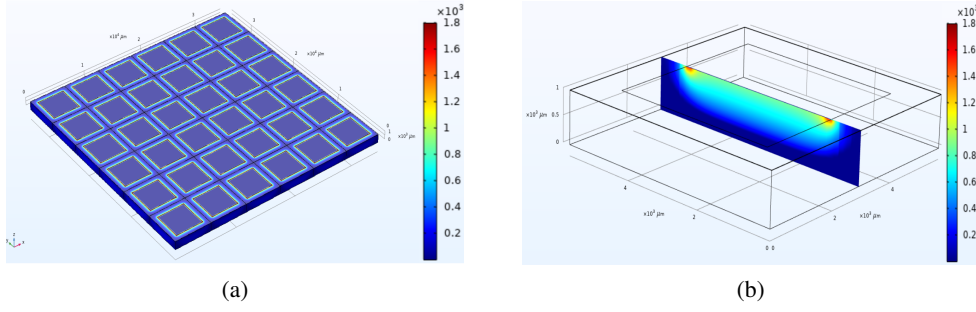


Figure 4: (a) Visualization, in the three-dimensions, of the magnitude of the electric field [V/cm], throughout the volume of the germanium sensor under study, simulated using COMSOL Multiphysics®. (b) Cross-section through the sensor volume shows the magnitude of the electric field through one single pixel.

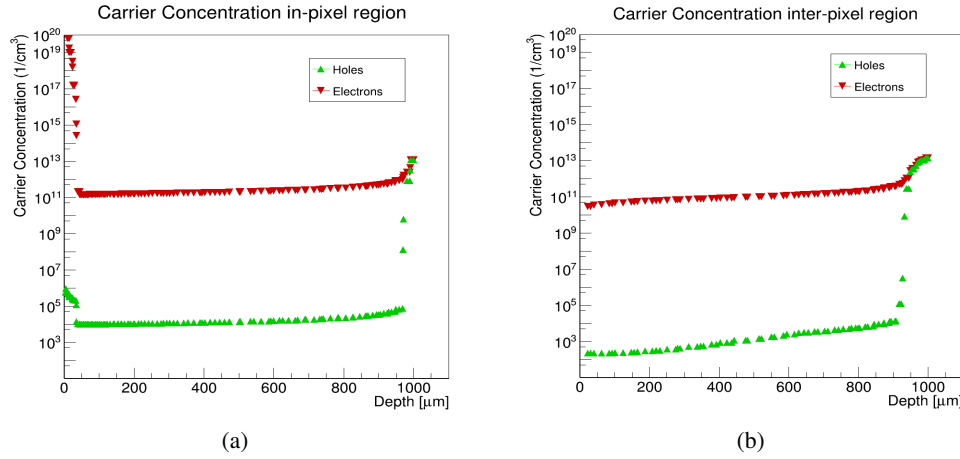


Figure 5: Charge Carrier concentration as a function of depth for the in-pixel region (a) and inter-pixel region (b). In both plots, the axis reference is situated at the segmented side (pixels), while the max depth is situated at the front implanted side.

Additional COMSOL simulation has been performed to take into account the induced charge on the electrode resulting from a charged particle moving near the electrode. This can be quantified using the Shockley-Ramo Theorem and weighting potential can be calculated. The weighting potential is a unit-less potential found by setting the electrode for which we want to calculate the induced charge to 1 and all others to 0. With these boundary conditions, the same procedure described previously in this section was followed to calculate the weighting potential. The resulting weighting potential maps are shown in Figure 6.

Finally, in order to export electric field and weighting potential maps into allpix-squared, a grid (.grd) file containing the adaptive mesh and the evaluated electric field components in three dimensions has been generated directly within the COMSOL interface. The adaptive COMSOL mesh should be interpolated and transformed into a regular grid with a configurable feature size

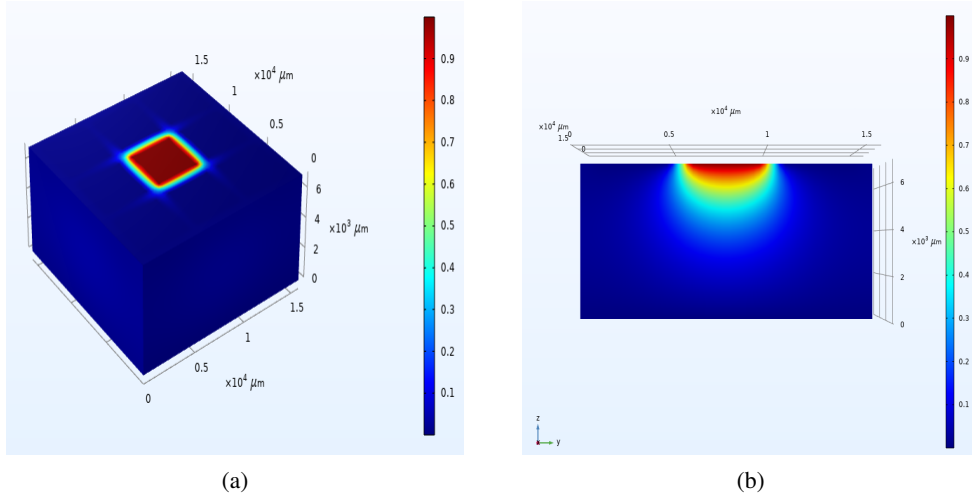


Figure 6: (a) Three-dimensional map of the simulated weighting potentials for the germanium sensor under study and (b) two-dimensional weighting potential slice in plan perpendicular to the detector surface.

before use in allpix-squared. For this purpose, a script has been written to convert these .grd files into a .init file (one of the supported field file formats to read field maps in allpix-squared), and to extrapolate a linear electric field map over the remaining depth up to complete the 7 mm thickness. Then, the output .init file is imported into allpix-squared for next simulation step.

3.3 Charge carrier drift and signal induction

Charge carriers are propagated along the electric field lines through the germanium crystal until front and back sides by the *GenericPropagation* module. This module uses a Runge-Kutta integration method and the mobility is calculated at each step from the interpolated vector obtained from the three dimensional electric field map, imported by the *ElectricFieldReader* module. Random diffusion is added to every integration step of the charge carrier motion using Fick's second law and Einstein relation. The drift mobility parameterization in germanium at 77 K is formally the same as in silicon, but the parameter values have been modified to those measured along the principal crystallographic axis $\langle 100 \rangle$ for electric fields lower than 300 V/cm [11]. The drift velocity anisotropy, observed in relatively thick (i.e. 7 cm) germanium detectors [12], is small for thin sensors like in our case and has not been included in the simulation.

Charge carriers are propagated during 200 ns, the so-called *integration time*. In this work, the *InducedTransfer* module is used to combine the individual sets of propagated charges together to a set of charges on the sensor pixels by calculating the total induced charge during their drift on neighboring pixels by calculating the difference in weighting potential. Using this module, all propagated charges, within the specified integration time, are taken into account and the resulting induced charge is summed for all propagated charge carriers. The integration time has been chosen long enough so that charge carriers are collected either to the electrodes or any other germanium surface. It has been verified that by drifting the charge carriers in groups of 100, with the integration

time per step set to 1 ns, both to speed up the simulation process, simulation results are precise enough in terms of energy spectrum shape and charge carrier arrival time distribution.

3.4 Signal digitization and energy spectrum

Charge carriers accumulated around the pixel electrodes are transformed into a digital signal using the *DefaultDigitized* module. The applied threshold to each pixel has been fixed to 100 e^- . The electronics noise is modeled by a Gaussian distribution centered at zero with a standard deviation of 31 e^- , equivalent to an energy resolution (FWHM) of 235 eV at an X-ray energy of 5.9 keV and an integration time of 1 μs . This value has been experimentally measured and has been cross-checked by a detector noise model [13].

While the main DPP features, i.e. dead time and time resolution, are not yet modeled in the current allpix-squared version of v1.6.0 [14], these features have been modeled in an offline analysis. The dead time is the mean time for a DPP to digitize the signal amplitude. The time resolution models pile-up effects, i.e., the efficiency to resolve two close induced signals in time. These two parameters are basically defined by the type of digital filter [15]. Values of 1430 ns for measurement time and of 300 ns for time resolution have been set based on experimental data of a germanium detector equipped with XIA-DXP-xMAP DPP [16].

Simulation results are stored in ROOT [17] trees using the *ROOTObjectWriter* module. For each simulated event, the information of the deposited charge carriers and the fired pixels (*PixelHit*) is stored. The number of absolute simulated X-rays varies between 5×10^7 photons per value of energy in the case of the direct beam, equivalent to an exposure time of around 140 s at a photon flux of $3.6 \times 10^5\text{ ph/sec}$ to 2×10^{11} photons in the case of sample irradiation, equivalent to an exposure time of around 6 sec for a photon flux of $3.47 \times 10^{10}\text{ ph/sec}$.

4 Simulation of multi-element germanium detector performance

The performance of a semiconductor particle detector is strongly affected by the charge transport properties of the sensor material. Diffusion, in particular, and drift of electrical charges is a main concern in the case of pixelated detectors. A part of the charge created in the sensor volume may be shared between neighboring pixels as explained in section 3; it is the charge sharing effect. This effect is undesirable in radiation detectors since it leads to the underestimation of the energy of incident photons, and as a result, it reduces the signal efficiency. Moreover, the presence of charge sharing effect can seriously degrade the spectral resolution.

In this section, a study of the charge sharing effect in the germanium detector under study is presented, where all results shown have been obtained using the simulation chain presented earlier in this paper.

Moreover, current detectors in synchrotron experiments, e.g. Silicon Drift detectors (SDD) and germanium detectors, use an internal collimator to avoid border area events and to remove almost charge sharing effect. On one hand, using the collimator can be seen as a simple and efficient solution to improve the signal-to-background ratio. On the other hand, using it implies a significant reduction of the detector active area, especially for photons with small incident angles. In the future, synchrotron light sources will produce more intense photon beams and detectors with higher granularity and smaller pixel size will be required. However, from a technical point of view,

Table 2: Summary of simulation conditions used to obtain the results for the charge sharing study.

Simulation Conditions	
Number of simulated events	50 M
Beam energy	30 keV
Beam shape	Squared
Beam size	$30 \times 30 \text{ mm}^2$
Beam direction	Z-axis (perpendicular incidence)
Particle type	Photon
Source distance	5 cm

it could be difficult to have collimators that fit smaller pixel sizes and the resulting dead area could become a serious limitation of granular detectors. For these reasons, it is interesting to compare performance of germanium detectors with or without using a collimator.

4.1 Quantification of the charge sharing effect with and without collimator

In this section, the charge sharing effect is evaluated using two variables: the cluster size and the seed charge. The cluster is defined as the set of pixels that are fired when one photon is interacting with the detector. Hence, the *cluster size* is equal to the number of pixels belonging to a cluster. The *seed signal* is defined as the ratio between the charge of the pixel, in which the incident particle deposited its energy, and the total charge. The simulation conditions used to obtain the following results in this section are summarized in Table 2.

The distribution of the cluster size for the germanium detector with collimator is presented in Figure 7 (a). The cluster size multiplicity shows that the large majority of the events have a cluster size equal to 1 (these are events that are collected in a single pixel). Less than 2.8% of the events are contributing to the charge sharing effect in this case. This result illustrates the important role of the collimator in removing the charge sharing effect. The 2D map in x and y, depicted in Figure 7 (b), provides more details on the cluster size spatial distribution. The largest cluster size occurs at the pixel corners, as expected, since the high electric field present in this area results in a strong contribution from drift of charge carriers. As a consequence, the induced charge carriers of one pixel can easily diffuse into adjacent pixel cells, resulting in a cluster size of 2 to 4 in the corner. On the other hand, the cluster size is 1 at the center of the pixel because charge carriers are unlikely to diffuse to neighboring pixel cells.

Figure 8 (a) shows the seed signal map in x and y and depicts a decrease of the seed signal towards the edges due the presence of the collimator. A scan of the seed signal along a horizontal cut-line crossing the middle of a pixel row is shown in Figure 8 (b) in which the seed signal drops down to 10% of the maximum in the inter-pixel region, while the vertical lines represent the error bars for each data point.

The charge sharing effect can also be quantified by measuring the charge sharing region extension defined as the region where the signals from the two neighbor pixels are below 90% on both sides, i.e. the charge is shared. The charge sharing region extension is calculated from Figure 9, where a pixel charge scan is done between two adjacent pixels. In the case where there is no collimator (Figure 9 (b)), a Gaussian fit is used to estimate the charge sharing region extension.

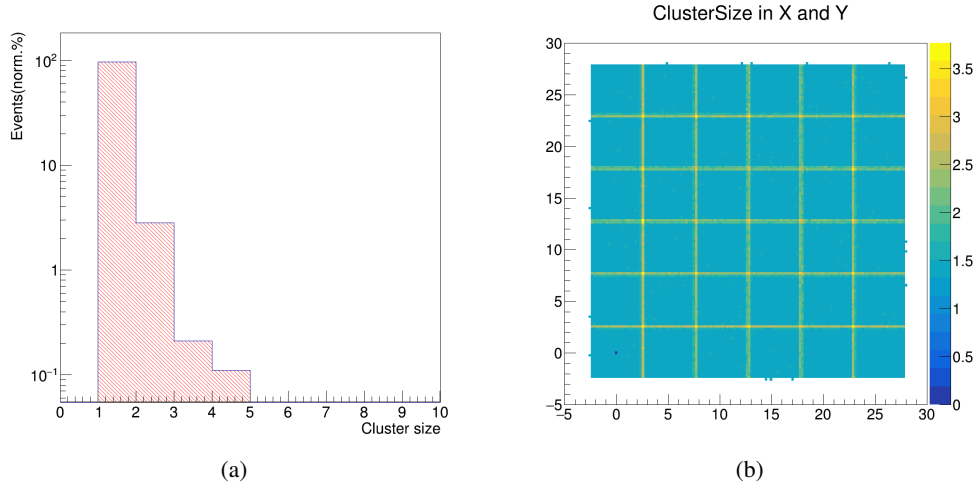


Figure 7: Cluster size distribution (a) and cluster size map (b) for the multi-element germanium detector under study with collimator.

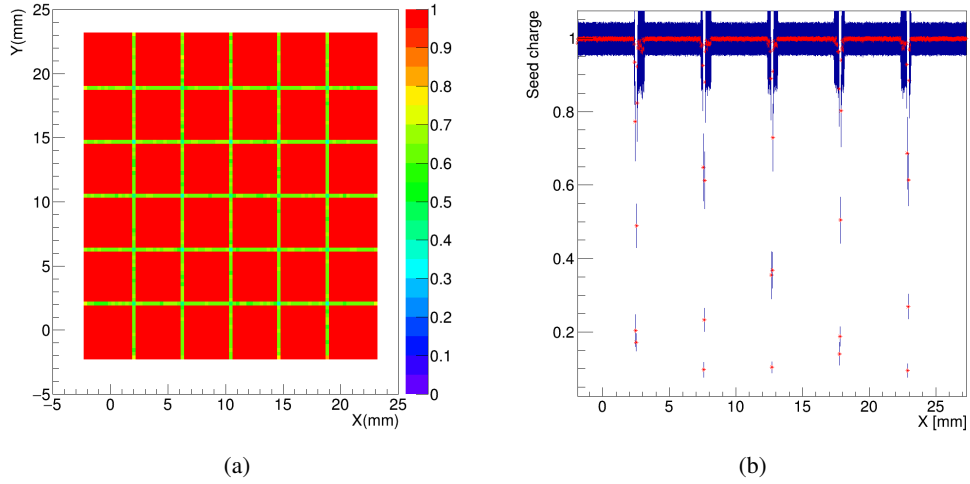


Figure 8: (a) Seed signal map and (b) seed signal distribution along a horizontal cut-line crossing the middle of a pixel row for the multi-element germanium detector under study with collimator.

In both cases, the pixel charge scan shows that in the inter-pixel region, the pixel charge drops down to about 10% - 20% of the total signal. The charge sharing region extension is measured to be $114 \mu\text{m}$ when removing the collimator, which is much smaller than the inter-pixel gap of $800 \mu\text{m}$. When the collimator is present, the dead area results in an inefficiency width of 1.0 mm, which is larger than the inter-pixel gap. This means that the pixels are well isolated for detector design with collimator but at the same time, this causes a significant reduction of the active area of about 30%. Hence, removing the collimator, in these conditions, can be a good strategy to increase the active area in some experiments.

Summary of the different observables used to quantify the charge sharing effect and to study

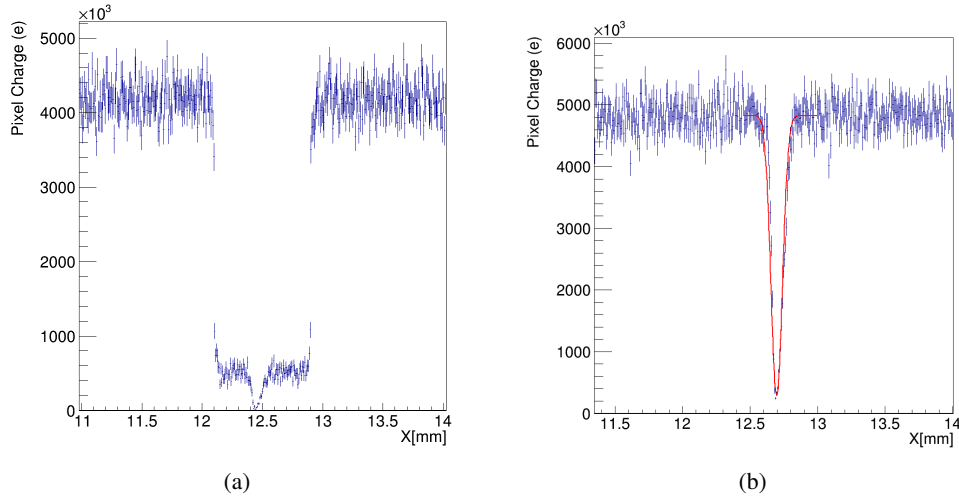


Figure 9: Pixel charge scan, along a horizontal cut-line crossing the middle of a pixel row, for the multi-element germanium detector under study with collimator (a), without collimator (b).

Table 3: Summary of the different parameters and their corresponding values found in this study.

Parameter	Detector With Collimator	Detector Without Collimator
Pixel Size [mm^2]	4.2×4.2	4.2×4.2
Detector Sensitive Area [mm^2]	635	820
Sensor Thickness [mm]	7	7
Shared events [norm. %]	3%	8%
Signal efficiency (%)	95%	88%
Background efficiency (%)	0.04%	0.50%
Signal-to-Background ratio	2375	180
Charge sharing width [μm]	1003	114

the multi-element germanium detector response, with and without collimator, can be found in Table 3 and results are explained in more details in the next section.

4.2 Study of the detector performance at different beam energies

Further simulations have been performed to study the performance of the germanium detector under study with and without Ti collimator at different beam energies between 5 and 80 keV. As shown in the previous section, a uniform photon beam perpendicular to the detector frontside has been considered. In this section, the different simulation results are presented, in particular the number of shared events and the signal-to-background ratio (S/B).

The S/B ratio is defined as the number of events in a signal RoI (Region of Interest) divided by the number of events in the background RoI as illustrated in Figure 10, where an incident photon beam energy of 28 keV is used in this example. In the energy spectrum, the signal RoI is defined at the position of the photoelectric peak in the range $[E_{photo} - 0.5, E_{photo} + 0.5]$ keV, while the background RoI is defined in the Compton level in the range $[E_{photo} - 4, E_{photo} - 3]$ keV. For this

study, all pixels with energy less than 1 keV have been excluded since all the digital electronics, e.g. X-MAP, FalconX and Xspress3 that are used during experiments on the beamline, currently apply this cut on energy. Therefore, this selection has been applied in order to have a better agreement later on between data and simulation.

Figure 11 (a) shows the S/B ratio as a function of the beam energy. This result shows that the S/B ratio is strongly dependent on the energy of the incident photon only for with-collimator configuration, while the dependence is smoother in absence of a collimator. S/B is higher for a with-collimator design for all beam energies < 60 keV. For beam energies > 60 keV, the S/B for both configurations is nearly the same showing that the collimator has no longer a significant effect at high energy and becomes transparent to incident photons. In both cases (with and without collimator), an abrupt drop of the S/B ratio is observed between 10 and 15 keV, due to the loss of signal efficiency related to the presence of K_α and K_β emissions lines of germanium, as already observed in other studies [18].

The number of shared events as a function of beam energy is shown in Figure 11 (b). This study shows that the number of shared events increases for higher beam energies in both configurations. At energies lower than 20 keV, the collimator helps in removing almost completely all shared events. In the configuration without collimator, the number of shared events shows a plateau in the energy range 30 and 60 keV, as charge sharing is mainly determined by *splitted events* and this number does not change with energy. In fact, the size of charge cloud increases with energy but photons are also absorbed deeper and closer to the pixel implant, which counteravails the other effect [19]. Meanwhile, at energies higher than 60 keV, the number of shared events increases as it is mainly determined by *fluorescence events*, i.e., photons absorbed in one pixel and one escaping fluorescence photon absorbed in another pixel. In both cases, the number of shared events increases up to 10% at 80 keV.

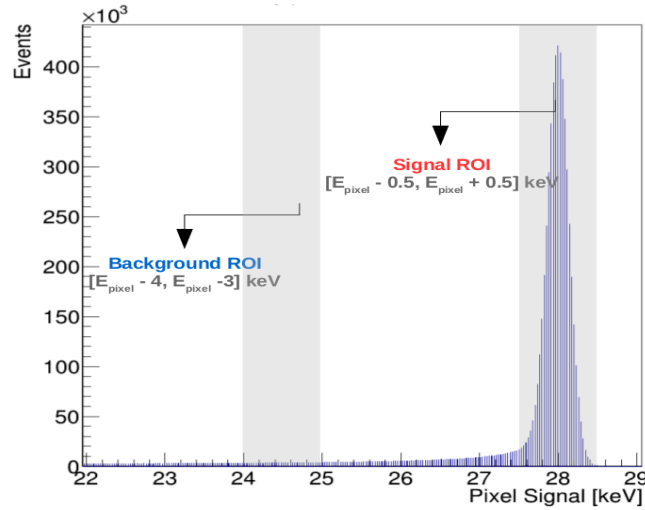


Figure 10: Energy spectrum for a photon beam of energy 28 keV shows the signal and background ROI regions defined for this study. Shaded areas define the boundaries of the different ROI regions.

The results herein obtained shows that the simulation chain proposed in this paper is fully operational and allowed us to quantify some interesting performance parameters of the multi-

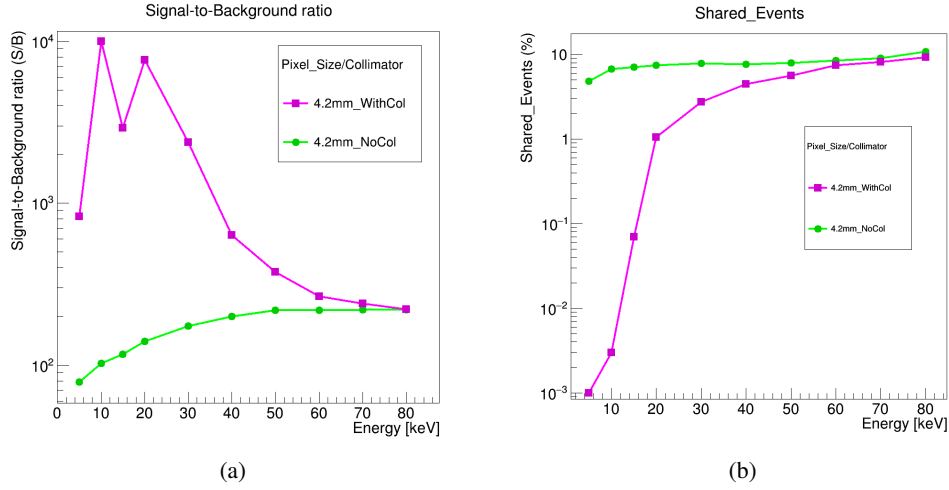


Figure 11: Signal-to-background ratio (a) and number of shared events (b) as a function of incident photon beam energy for the detector with and without collimator.

element germanium detector under study. Further studies and detector design improvement can benefit from using these simulation tools.

5 Experimental measurements to calibrate simulation results

In order to calibrate and prove that the simulation chain proposed in this paper is reliable, a comparison between simulation and experimental data, in a particular cases, has been performed and is presented in this section. The experimental data were recorded at the SAMBA beamline of SOLEIL synchrotron using the germanium detector under study, previously described in Section 2. During the on-beamline measurement, an energy spectrum of 60 seconds acquisition time has been recorded for each of the 36 active pixels of the detector and using the XIA-DXP-XMAP DPP.

5.1 On-beamline measurements

Two different measurements have been performed at the SAMBA beamline. The first one, illustrated in Figure 12 (a) and (b), was a typical fluorescence measurement of a complex sample, with the aim at reproducing with our simulation all the X-ray lines emitted by this sample. In the second measurement, illustrated in Figure 13 (a) and (b), the objective was to study multi-element germanium detector performance in the inter-pixel region by performing a horizontal scan using a collimated beam and compare results from measurement to simulation. The two setups were therefore very different and are described below:

- **Experimental measurement with a Cadmium (Cd) sample and wide detector illumination:** for this measurement, a well-known sample composed of Cadmium (0.918 %), Iron (0.26%), and traces of Lead (20 ppm), Strontium (30 ppm), Zirconium (20 ppm), and Copper (3 ppm) has been used. The energy of the beam was set to 28.0 keV by a monochromator situated upstream of the beamline. The beam size was then focused in a small area at the sample spot ($385 \mu\text{m} \times 250 \mu\text{m}$ widths in the horizontal and vertical axis) and a photon flux

of 3.47×10^{10} ph/sec was measured by the ionization chamber situated just before the sample. Then, a cylindrical sample (10 mm diameter, 1.0 mm thick, a density of 1.28 g/cm^3) was placed at the sample spot, at an angle of 45 deg between the beam and the detector, and the germanium detector was moved forward to reach a sample-to-detector distance of 312 mm, corresponding to an input count rate of ~ 28 kcps and a dead time of $\sim 13\%$ measured for all pixels. In this case, this dead time value is small enough to keep a linear relationship between an element concentration and the sum of measured X-rays fluorescence intensities at germanium detector pixels. The setup of this measurement is shown in Figure 12 (a) and (b).

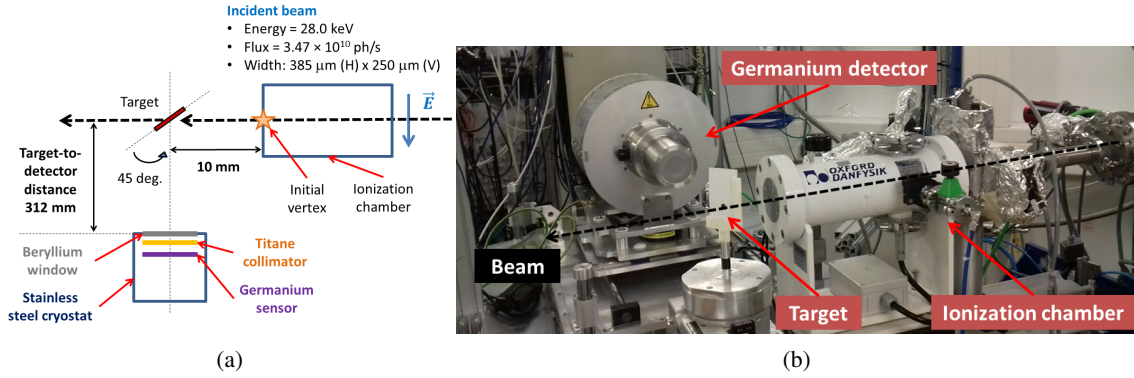


Figure 12: (a) General layout of a typical on-beamline measurement at the SAMBA beamline. (b) Picture of the whole experimental setup used for fluorescence measurement.

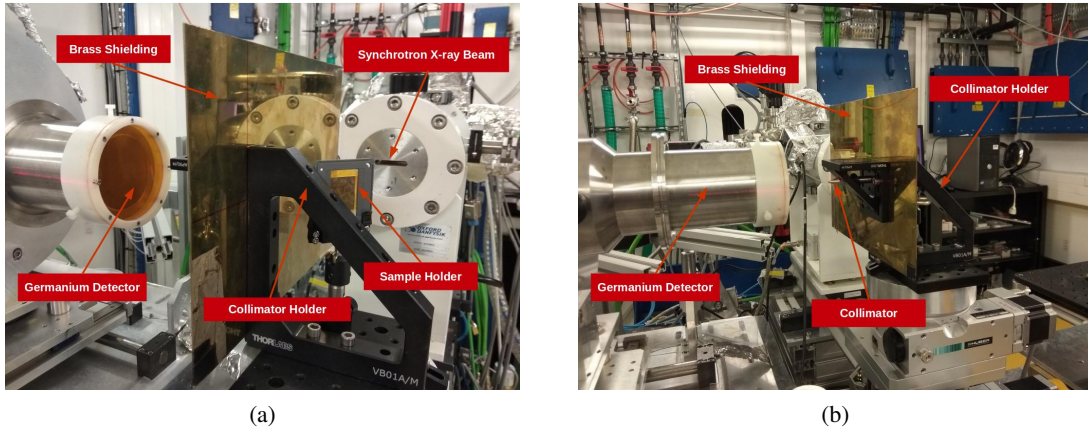


Figure 13: (a) Experimental setup used for the charge sharing effect investigation at the SAMBA beamline and (b) another view of the setup shows the collimator placed between the germanium detector and the sample holder.

- **Experimental measurement with a Tin (Sn) foil and collimated detector illumination:** this second measurement aimed at studying the charge sharing effect between two adjacent pixels. To achieve this objective, the previous experimental setup has been modified, as shown

in Figure 13 (a). In this setup, a collimator of 1 mm diameter, placed between the germanium detector and the sample holder at 5 mm distance from the detector, is used (see Figure 13 (b)). The collimator of 1 mm diameter allowed collimating the fluorescence emitted by a Sn foil in order to investigate the inter-pixel region and consequently the charge sharing effect. In addition, a plate of Brass has also been used to enhance shielding around the collimator. Similar to the previous measurement, the Sn foil is set at 45 deg between the beam and the detector, then necessary beam settings (energy, size, etc..) and alignment of the different components (i.e. beam spot, angle, collimator, and detector) has been done before starting measurements. Several horizontal scan of one row composed of 6 pixels has been performed with a step size of 0.2 mm.

5.2 Comparison between simulation and experimental results

For the first experiment with the Cadmium sample, a comparison of measured and simulated energy spectra is shown in Figure 14 represented in log scale. A rather fair agreement between data and simulation is observed, especially for the main X-ray lines of the chemical elements Cadmium, Iron, Strontium and Zirconium, and also the escape peaks of Cadmium X-ray emission lines. Despite the good agreement for the X-ray emission lines of the elements, we can notice two differences between experimental and simulated spectra:

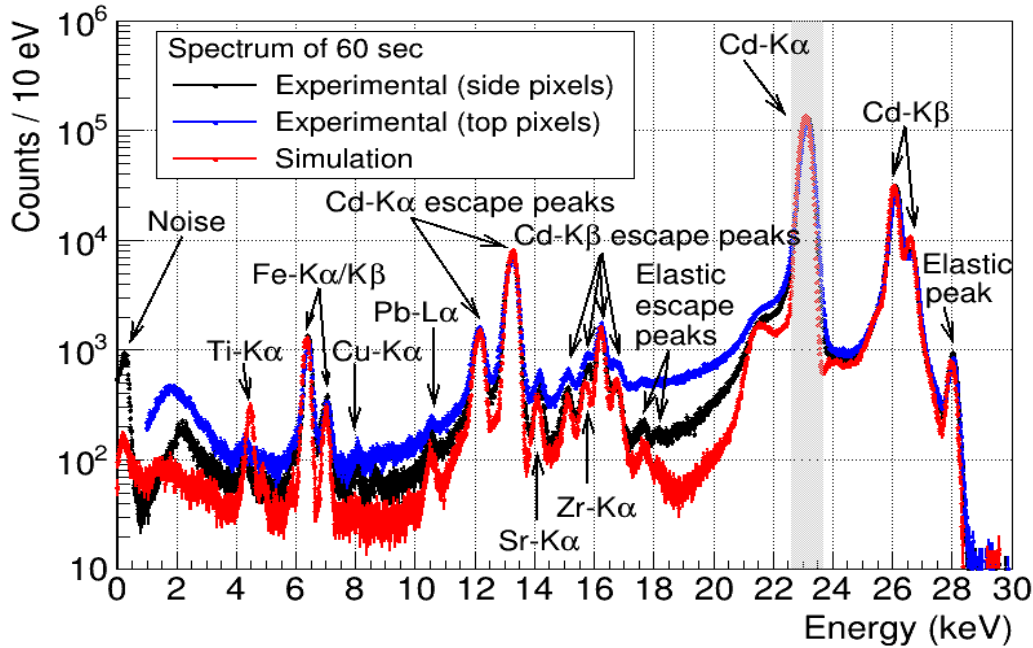


Figure 14: Simulated and measured energy spectrum from the on-beamline measurement with Cd sample at the SAMBA beamline. The simulated energy spectrum (red) is compared to two experimental spectra measured on two different pixels around disconnected pixels to show the dependence of the Compton level on the pixel's position.

- The Compton level of the Cadmium line (energies lower than 20 keV), is higher in experimental data. This is due to the fact that the Compton level of experimental data includes an extra contribution by preamplifier reset signals, which has not been yet modeled in our simulation. Moreover, the detector used in the measurements had some disconnected (noisy) pixels while our simulation assumes a perfect detector. As a result, the Compton level seems correlated to the pixel distance to the two disconnected pixels situated at the top part of the germanium sensor. This dispersion of Compton level along the sensor surface is illustrated by the energy spectrum of 6 pixels around the disconnected ones (blue curve). The side pixels (black curve) feature a better agreement with simulated spectra on the Compton level.
- The presence of Titanium fluorescence X-ray emission lines (at 4.51 and 4.93 keV) in the simulation, while they are absent in real data. The Titanium collimator is certainly coated with aluminum to block its fluorescence lines as cited here [20]. This coating has not been included in the detector model due to the absence of information in the datasheet of the detector.

Regarding the second experimental measurement, the multi-element germanium detector performance in the inter-pixel region has been investigated. Thanks to a collimated beam emitted from the Sn foil, the intensity of the K_α line of Sn (i.e. total number of counts around the K_α peak of Sn, in the RoI [24.7 keV - 25.7 keV] has been studied as a function of the horizontal position and shown in Figure 15.

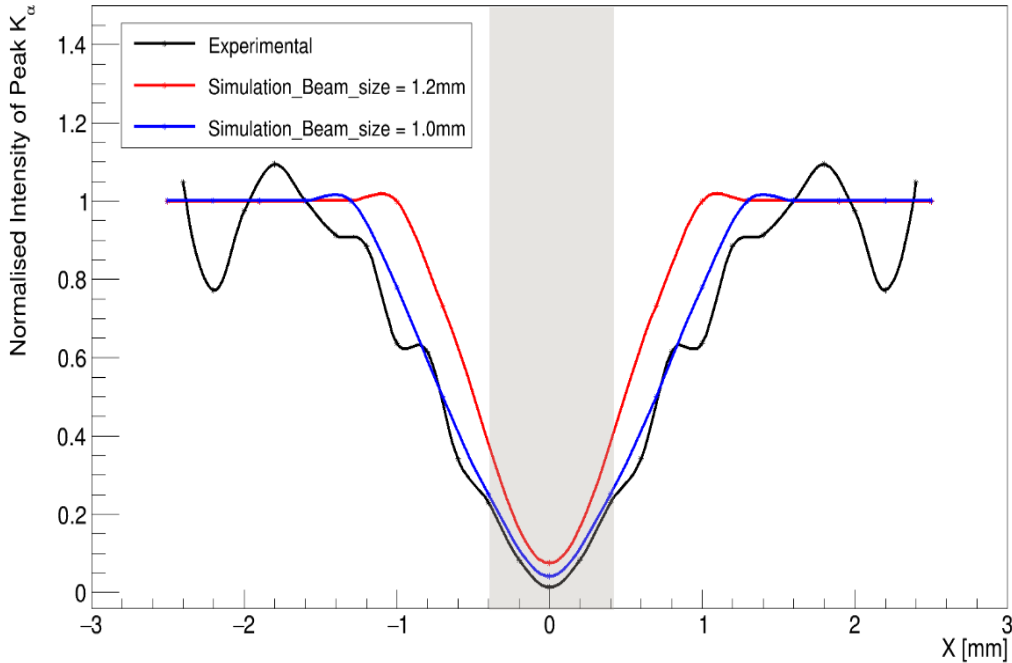


Figure 15: The intensity of the K_α line as a function of horizontal scan position. Comparison between simulation and on-beamline measurement with Sn foil at the SAMBA beamline. The shaded area define the limits of the inter-pixel region.

This figure shows a comparison of the normalized intensity of the K_α line with experimental data and simulated data, corresponding to two different beam diameters (1.0 mm and 1.2 mm). These results show that the better agreement is obtained for the simulated beam of 1 mm diameter, which is coherent with a collimator size of 1 mm that is used during this measurement as explained previously in section 5.1. The intensity of the K_α line increases slightly for a larger beam size of 1.2 mm. This can be explained by the fact that as the beam spot getting larger, it is covering a larger area. Also, using the weighting potential map as well as the induced charge transfer module in simulation, more hits can be collected and identified. In the inter-pixel region, the number of counts (hits) is negligible ($\approx 5\%$ of the maximum intensity) and a good agreement between simulation and measurement is observed. We can also notice some oscillation in the experimental data that could be explained by the non-uniformity of the incident beam (unfortunately not measured during the experiment) and the non perfect stability of our detector mechanical motorized table after each scan step. Despite those small differences explainable, we conclude that our simulation chain is fully operational and is working quite well.

6 Conclusion and Outlook

This work presents for the first time a complete and operational simulation chain specifically dedicated to multi-element germanium detectors. The simulation is mainly based on allpix-squared simulation customized to study the performance of germanium detectors. For a realistic modeling of the detector performance, allpix-squared simulation has been combined with a 3D electrostatic field simulation based on COMSOL Multiphysics®.

Using this simulation chain, a quantification of charge sharing effect as well as signal-to-background ratio studies at different beam energies for a multi-element germanium detector were presented.

Results show that charge sharing is strongly dependent on incident photon beam energy as expected. In the presence of a collimator, a cluster size is equal to 1 for almost all the events, while removing the collimator results in 8% additional events contributing to cluster size >1 . Using a collimator is very useful in removing the charge sharing effect, but in the same time, it decreases the detector sensitive area. In the absence of a collimator, the charge sharing region extension, found by simulation, is about $114 \mu\text{m}$. In this case, the detector sensitive area is increased by about 30% which is not negligible.

Studies of the detector performance at different beam energy (5-80 keV) show that the S/B ratio is firmly energy-dependent for the with-collimator configuration. In this case, S/B is high (of the order of 1000) at low energy up to 30 keV. Then, at higher energies, the S/B ratio drops down to 500 at 50 keV. On the other hand, the no-collimator configuration shows a slight increase in the S/B ratio which is of the order of 100 for all energies 5-80 keV. Finally, the number of shared events tends to increase as beam energy increases for both cases, i.e., with and without collimator configurations. At low energy, the number of shared events is negligible up to 20 keV for the with-collimator configuration. On the contrary, the no-collimator configuration shows a significant percentage of shared events up to about 6% at low energy. In both cases, the number of shared events increases up to 10% at 80 keV.

In addition, various experimental measurements have been performed on the SAMBA beamline at SOLEIL synchrotron. The experimental data were used to calibrate the full simulation chain and, rather good agreements have been observed between data and simulation.

This simulation chain provides a powerful tool that could drive current and future developments of new generations of multi-element germanium detectors. Further studies to investigate the detector performance in different configurations are ongoing, i.e. for smaller pixel sizes and different pixels geometries. These studies will aim at optimizing the detector design, in order to enhance the S/B ratio for detecting chemical species with very low concentrations (< 10 ppm).

Scientific cases of XAFS experiments could also be studied, such as detecting heavy element traces, like Cadmium or Lead, over a background level created by the beam X-rays (and commonly known as elastic peak), or light elements in a complex sample, whose background level is mainly defined by the Compton level of more intense fluorescence lines situated at higher energy.

Acknowledgments

The authors acknowledge E. Fonda and G. Landrot, both scientists of the SAMBA beamline at SOLEIL synchrotron, for their cooperation in providing beamtime and information about the samples used during the measurement performed on the SAMBA beamline. The authors would like also to thank SOLEIL computing service (ISI), in particular to Ph. Martinez, for technical support in the use of SUMO and COBALT IT clusters.

References

- [1] W.L. Hansen. High-purity germanium crystal growing. *Nucl. Instrum. Meth. A*, 94(2):377 – 380, 1971. ISSN 0029-554X. doi: [https://doi.org/10.1016/0029-554X\(71\)90593-3](https://doi.org/10.1016/0029-554X(71)90593-3). URL <http://www.sciencedirect.com/science/article/pii/0029554X71905933>.
- [2] P. Sangsingkeow et al. Advances in germanium detector technology. *Nucl. Instrum. Meth. A*, 505(1): 183 – 186, 2003. ISSN 0168-9002. doi: [https://doi.org/10.1016/S0168-9002\(03\)01047-7](https://doi.org/10.1016/S0168-9002(03)01047-7). URL <http://www.sciencedirect.com/science/article/pii/S0168900203010477>. Proceedings of the tenth Symposium on Radiation Measurements and Applications.
- [3] M. Amman. Optimization of Amorphous Germanium Electrical Contacts and Surface Coatings on High Purity Germanium Radiation Detectors. 9 2018. doi: 10.13140/RG.2.2.34748.08327/1.
- [4] S. Spannagel et al. Allpix² : A modular simulation framework for silicon detectors. *Nucl. Instrum. Meth. A*, 910:164–172, 2018.
- [5] E. Fonda et al. The samba quick-exafs monochromator: Xas with edge jumping. *Journal of Synchrotron Radiation*, 19(3):417–424, 2012. doi: <https://doi.org/10.1107/S0909049512009703>.
- [6] J. Barylak et al. Simulation of charge sharing in the caliste-so detector. *Nucl. Instrum. Meth. A*, 903: 234–240, 2018. ISSN 0168-9002. doi: <https://doi.org/10.1016/j.nima.2018.05.062>.
- [7] S. Agostinelli et al. GEANT4: A Simulation toolkit. *Nucl. Instrum. Meth. A*, A506:250–303, 2003. doi: 10.1016/S0168-9002(03)01368-8.
- [8] G. Cirrone et al. Validation of the geant4 electromagnetic photon cross-sections for elements and compounds. *Nucl. Instrum. Meth. A*, 618(1-3):315–322, 2010. ISSN 0168-9002. doi: 10.1016/j.nima.2010.02.112.

- [9] S.O.W. Antman et al. Measurements of the fano factor and the energy per hole-electron pair in germanium. *Nucl. Instrum. Meth. A*, 40(2):272–276, 1966. ISSN 0029-554X. doi: 10.1016/0029-554X(66)90386-7.
- [10] Y. Okuto and C. R. Crowell. Threshold energy effect on avalanche breakdown in semiconductor junctions. *Solid-State Electronics*, 18:161–168, 1975.
- [11] B. Bruyneel et al. Characterization of large volume hpge detectors. part i: Electron and hole mobility parameterization. *Nucl. Instrum. Meth. A*, 569(3):764 – 773, 2006. ISSN 0168-9002. doi: <https://doi.org/10.1016/j.nima.2006.08.130>.
- [12] I. Abt et al. Pulse shape simulation for segmented true-coaxial HPGe detectors. *Eur. Phys. J. C*, 68: 609–618, 2010. doi: 10.1140/epjc/s10052-010-1364-9.
- [13] M. Bordessoule. The relation between the output spectral noise and the energy resolution of the canberra 36 elements of samba. *Tech. Rep., EXP-DET20-R009-A, Synchrotron SOLEIL*, 2020.
- [14] S. Spannagel et al. Allpix Squared - Generic Pixel Detector Simulation Framework. *Zenodo*, October 2020. doi: 10.5281/zenodo.4494619. URL <https://doi.org/10.5281/zenodo.4494619>.
- [15] M. Bordessoule et al. Performance of spectroscopy detectors and associated electronics measured at soleil synchrotron. *AIP Conference Proceedings*, 2054(1):060070, 2019. doi: 10.1063/1.5084701.
- [16] B. Hubbard et al. Digital x-ray processing electronics for fluorescence exafs and spectroscopy. *Rev. sci. Instrum.*, 67(9):3371, 1996. doi: 10.1063/1.1147335.
- [17] R. Brun and F. Rademakers. ROOT: An object oriented data analysis framework. *Nucl. Instrum. Meth. A*, 389:81–86, 1997. doi: 10.1016/S0168-9002(97)00048-X.
- [18] S. Deloule et al. Determination of the efficiency of high purity germanium and silicon diode detectors for improved assessment of emission spectra delivered by medical X-ray tubes. *X-Ray Spectrometry*, 42(4):201 – 206, July 2013. doi: 10.1002/xrs.2471. URL <https://hal-cea.archives-ouvertes.fr/cea-01791938>.
- [19] J. Barylak et al. Simulation of charge sharing in the Caliste-SO detector. *Nucl. Instrum. Meth. A*, 903: 234–240, 2018. doi: 10.1016/j.nima.2018.05.062.
- [20] S. Chatterji et al. Overview of multi-element monolithic germanium detectors for xafs experiments at diamond light source. *AIP Conference Proceedings*, 1741(1):040030, 2016. doi: 10.1063/1.4952902.